Elastohydrodynamic autoregulation in soft overlapping channels

Magnus V. Paludan, Matthew D. Biviano, and Kaare H. Jensen[*]
Department of Physics, Technical University of Denmark, 2800 Kongens Lyngby, Denmark

Controlling fluid flow from an unsteady source is a challenging problem that is relevant in both living and man-made systems. Animals have evolved various autoregulatory mechanisms to maintain homeostasis in vital organs. This keeps the influx of nutrients essentially constant and independent of the perfusion pressure. Up to this point, the autoregulation processes have primarily been ascribed to active mechanisms that regulate vessel size, thereby adjusting the hydraulic conductance in response to, e.g., sensing of wall shear stress. We propose an alternative elastohydrodynamic mechanism based on contacting soft vessels. Inspired by Starling's resistor, we combine experiments and theory to study the flow of a viscous liquid through a self-intersecting soft conduit. In the overlapping region, the pressure difference between the two channel segments can cause one pipe segment to dilate while the other is compressed. If the tissue is sufficiently soft, this mode of fluid-structure interactions can lead to flow autoregulation. Our experimental observations compare well to a predictive model based on low-Reynolds-number fluid flow and linear elasticity. Implications for conduit arrangement and passive autoregulation in organs and limbs are discussed.

I. INTRODUCTION

Fluid flow in soft conduits is ubiquitous, and it is well established that the deformation of individual channels can impact flow quantity and quality [1]. For instance, many animals, including mammals, have evolved autoregulatory mechanisms in which cardiovascular vessels expand and contract to maintain an approximately steady oxygen and nutrient supply [2–4]. This process is critical in sensitive organs such as the brain, kidneys, and liver, where constant perfusion rates are essential for homeostasis [5–7]. Presently, the feedback mechanism linking flow rates and conduit resistance is ascribed to active cellular processes that integrate the sensing of local shear and metabolic rates to actuate vascular muscles in myogenic processes [2,6,8].

It remains unclear, however, if a simpler and purely mechanical process could account for some of the observed flow autoregulation. The three-dimensional arrangement of veins and arteries may hold clues to such a mechanism. In some cases, veins and arteries that feed into and out of the same organ, or region of an organ, come into direct contact within a confined space [Fig. 1(a)]. Examples of such overlapping conduits can be found in or near the brain [9], spinal cord [10], penis [11], pelvis [12], and kidney [13].

Blood flow across organs, as mentioned earlier, is driven by a pressure difference Δp between the incoming artery and outgoing vein generated by the heart muscle [8]. If the pressure drop over the organ is sufficiently large, the two overlapping tubes have the potential to deform in such a way that the inlet conduit expands while the outlet contracts [Figs. 1(b) and 1(c)]. This increases the net hydraulic resistance of the

system, thus creating conditions suitable for a sublinear pressure drop versus flow rate relation. We hypothesize that this fluid-structure interaction could contribute to the observed autoregulation processes. This conjecture is further supported by the fact that similar interactions between overlapping pipes enable essential physiological processes, e.g., venous restriction during mammalian penile erection [11,14]. It is also worth noting that conduit proximity is involved in several medical conditions. The May-Thurner syndrome, where the right iliac artery and the left iliac vein overlap in the pelvis, can cause leg edema due to vein compression [12]. Similarly, in the nutcracker syndrome, the aorta and superior mesenteric artery compress the renal vein leading to hematuria and abdominal pain [15].

While the physiological (dis)advantages of proximal soft pipes are evident, the essential flow characteristics of soft *overlapping* conduits have received relatively little attention. Substantial research, however, has been conducted on *individual* flexible tubes (see, e.g., reviews by Pedley [16] and Heil and Hazel [1]). A notable example is the Starling resistor experiment in which a soft pipe is placed inside a sealed pressurized jacket [17–21]. This mimics, for instance, the action of extravascular muscles that act to either compress or expand flow vessels as part of the active control processes discussed previously. Flow limitation can occur in Starling's device if the jacket pressure increases proportionately to the pressure drop across the flexible conduit [22–24]. The detailed flow-rate characteristics depend, however, on the upstream, downstream, and jacket pressure and the geometrical and material parameters of the flexible soft tube, such as its length, radius, thickness, and stiffness. While Starling's resistor is relevant to the proposed autoregulatory mechanism, the detailed flow at the intersection between two connected overlapping channels has, to our knowledge, not been studied previously.
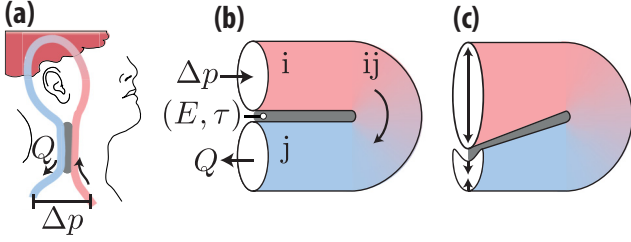
---

*khjensen@fysik.dtu.dk

FIG. 1. Fluid-structure interactions in a self-intersecting soft pipe. (a) Conceptual sketch of the blood supply to the human brain. The artery (red) that feeds into the brain overlaps with the vein (blue) that exits the brain. The artery and vein are connected via capillary beds in the brain. (b) The self-intersecting soft pipe connects in serial an inlet pipe (i), a connector pipe (ij), and an outlet pipe (j). The inlet (i) and outlet (j) overlap within the region marked by gray. The overlap has elastic modulus E, and the tissue thickness separating the conduits (i) and (j) is denoted τ. (c) If the pressure in pipe (i) exceeds the pressure in pipe (j), the elastic expansion of pipe (i) causes compression of pipe (j).

FIG. 2. Multilayered microfluidic device. (a) Photograph of the device. The internal structure is conceptually sketched. (b) Schematic (y, z) drawing of the device. (c) Schematical 3D drawing (x, y, z) of the device. Pressure is applied at channel (i)'s inlet, and channel (j)'s outlet is connected to ambient pressure.

In this paper we characterize the transport capacity of a self-intersecting soft channel using a combination of experiments and theory. We measure the flow-rate vs pressure-drop relation of a fluidic device that comprises two overlapping rectangular channels separated by an elastic sheet. The channels are connected via a resistive connector, mimicking the connecting organ or tissue. We vary the geometrical channel parameters (width and height), the sheet thickness, and the resistance of the connector. Our data indicate that purely passive autoregulation is possible in relatively soft overlapping channels when the organ resistance is not too large compared to the overlapping channels. On the other hand, if the channels are rigid or the organ resistance is too large, no flow control is observed. The experiments thus confirm the feasibility of the proposed passive autoregulatory mechanism if the overlap occurs relatively close to the target tissue. To rationalize our observations, we develop a theory based on low-Reynolds-number hydrodynamics and linear elasticity that capture the main system features. Finally, based on Murray's law, we estimate autoregulatory efficiency in human limbs and organs.

II. EXPERIMENTAL SETUP

This study aims to explore the hypothesis that fluid-structure interactions in a flexible self-intersecting conduit can autoregulate fluid flow (Fig. 1). To this end we have characterized pressure-driven flow in a multilayered fluidic device to quantify the flow in overlapping channels [Fig. 2(a)]. The device comprises two channels [(i) and (j)] that are serially connected via an internal resistor (ij) [Fig. 2(b)]. These three vessels correspond to the artery (i), vein (j), and organ (ij) (Fig. 1). An impermeable elastic sheet of thickness τ constitutes the soft shared boundary between channels (i) and (j). The transmural pressure, i.e., the pressure difference between channels (i) and (j), causes the sheet to deflect into the outlet channel (j), thereby reducing the channel height [see conceptual drawing in Figs. 1(b) and 1(c) and Fig. 2(c)]. Our fluidic device allows configuring the channel geometries, the
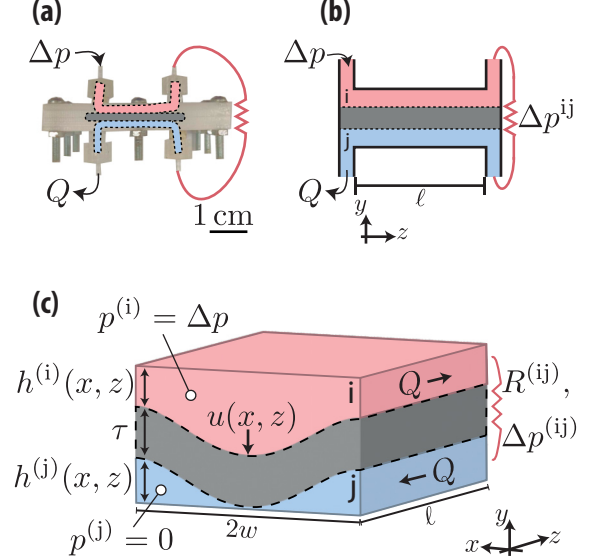
sheet material and thickness, and the magnitude of the organ resistance.

In our experiments, we measured the flow rate Q across the fluidic device by sweeping the applied pressure $\Delta p \approx$ 0–8 kPa at the inlet of channel (i). The outlet pressure of channel (j) was kept at atmospheric conditions. The system was allowed to equilibrate for 20 s and reach a steady state before measuring the flow rate at each step in the pressure sweep. Glycerol with viscosity $\mu = (1.2 \pm 0.1) \times 10^{-1}$ Pa s and density $\rho = (1.23 \pm 0.01) \times 10^3$ kg/m^3 was used as fluid. The pressure drop across the fluidic device was measured using two pressure sensors (26PC, Honeywell, USA) at the inlet and outlet of the device. The flow rate was measured using an electronic scale (Quintix124-1S, Sartorius, Germany).

The long and shallow rectangular overlapping channels were milled from a single piece of polyoxymethylene (Nomad 3, Carbide 3D, USA). We varied the channel height $h_0 = (251–325) \pm 25$ μm and width $2w = (2.1–2.4) \pm 0.1$ mm, while keeping the channel length $\ell = 30 \pm 1$ mm constant. The polymer sheet (Elite Double 22, Zhermack, Italy) with Poisson's ratio $\nu = 0.49$ [25] and elastic modulus $E = 363 \pm 58$ kPa (measured via a single cantilever beam test [26]) was clamped along the edges of the two overlapping channels. To explore the impact of vessel elasticity, we modified the membrane thickness $\tau = (0.40–1.00) \pm 0.05$ mm. To study the effects of organ resistance, we varied the interior resistor radius $a^{(ij)} = (0.25–2.00) \pm 0.10$ mm and resistor lengths $L = (5.9–18.5) \pm 0.5$ cm. To limit the effects of vessel compliance in the organ resistor, we used either relatively thick-walled silicone rubber tubings or polyetheretherketone tubing. The interior resistances were characterized by measuring the pressure-drop to flow-rate relationship via the method outlined above, and the hydraulic resistance was found by fitting a straight line to the pressure-flow

TABLE I. Parameters of microfluidic devices and network resistors used in the experiments. Each microfluidic device is assigned a color (column 5) and each network resistor a symbol (column 9). The following parameters were kept constant in the experiments: Channel length $\ell = 30 \pm 1$ mm, viscosity $\mu = (1.2 \pm 0.1) \times 10^{-1}$ Pa s, the membrane's Young's modulus $E = (363 \pm 50)$ kPa, and Poisson's ratio $\nu = 0.49$ [25].

Device	Channel height h_0 [μm]	Channel width $2w$ [mm]	Membrane thickness τ [μm]	Color	Resistor	Radius a [mm]	Length L [cm]	Symbol
1	251 ± 25	2.4 ± 0.1	400 ± 50	●	0	2.0 ± 0.1	8.0 ± 1.0	●
2	325 ± 25	2.4 ± 0.1	400 ± 50	●	1	0.25 ± 0.01	5.9 ± 0.5	■
3	223 ± 25	2.1 ± 0.1	400 ± 50	●	2	0.25 ± 0.01	11.7 ± 0.5	▲
4	233 ± 25	2.4 ± 0.1	1000 ± 50	●	3	0.25 ± 0.01	18.5 ± 0.5	◆
5	233 ± 25	2.4 ± 0.1	500 ± 50	●				

data. For clarity, we have assigned different colors and symbols to match each device and organ configuration. For an overview, see Table I.

III. RESULTS

Having outlined the experimental methods, we now focus on the observed pressure-drop vs flow-rate data. To contextualize our observations, we introduce two nondimensional variables critical to the hypothesized autoregulation mechanisms. For the elastic interactions between the two overlapping conduits to be significant in the overall flow capacity, the pressure difference across the elastic sheet must be sufficient to deform. From linear plate theory, we can estimate the pressure Δp_c required to deflect the membrane from its neutral position a distance h_0 until it contacts the bottom outlet channel as $\Delta p_c \propto E\tau^3 h_0/w^4$. The nondimensional pressure ratio

$$\tilde{P} = \frac{\text{APPLIED PRESSURE}}{\text{CONTACT PRESSURE}} = \frac{\Delta p}{\Delta p_c} \qquad (1)$$

quantifies whether the applied pressure is large enough to cause significant deformations ($\tilde{P}$ close to unity) or negligible deformations ($\tilde{P}$ close to zero). Even with significant outlet conduit compression, the internal or organ resistance (in our case, a rigid channel linking the two overlapping conduits) can dominate the overall flow characteristics if it is large compared to the summed resistance of the inlet and outlet channels. We quantify the nondimensional resistance by taking the ratio of internal or organ resistance ($R^{(ij)}$) to the sum of base (i.e., deformation-free) resistances of the inlet and outlet channels ($R_0^{(i)}$ and $R_0^{(j)}$)

$$\tilde{R} = \frac{\text{ORGAN RESISTANCE}}{\text{OVERLAP RESISTANCE}} = \frac{R^{(ij)}}{R_0^{(i)} + R_0^{(j)}}. \qquad (2)$$

In our experiments, the resistance ratio varies in the range $\tilde{R} = 10^{-4}$–10^1.

Experimental observations

We begin our discussion by considering the limit of a rigid shared boundary corresponding to a relatively thick membrane [Fig. 3(a)]. In this experiment, even when the resistance ratio is relatively small, $\tilde{R} \approx 10^{-4}$, we observe a linear ohmic relationship between the applied pressure Δp and the observed flow rate Q. For this device 4 (with

membrane thickness $\tau = 1.0$ mm, width $2w = 2.4$ mm, and height $h_0 = 0.23$ mm) we can estimate the contact pressure $\Delta p_c \approx 10$ kPa which is larger than maximum applied pressure $\Delta p = 7$ kPa in the experiment. Proceeding to consider deformations of the soft shared channel boundary, we examine a set of experiments using a relatively thin and/or wide membrane [Figs. 3(b) and 3(c)]. In these cases, sublinear relations between flow and pressure are observed. Notably, the regimes in which the flow rate is approximately constant, or varies slowly, as a function of applied pressure, correspond to successful autoregulation [Fig. 3(b)]. In contrast to device 4 [in Fig. 3(a)] device 1 [in Fig. 3(b)] has a thinner membrane (membrane thickness $\tau = 0.4$ mm, width $2w = 2.4$ mm, height $h_0 = 0.25$ mm), and we can estimate $\Delta p_c \approx 1$ kPa, consistent with the observed deviation from linear behavior at $\Delta p \approx 7$ kPa. To facilitate the subsequent discussion, we use device 1's contact pressure (i.e., $\Delta p_c^* = 7$ kPa) as a scale relative to which we contextualize all subsequent pressure data. For device 4, the contact pressure is larger than Δp_c^* because of the thicker membrane. In return, when the applied pressure reaches the baseline contact pressure, $\Delta p = \Delta p_c^*$, the pressure ratio is small compared to unity, and no digression from the 1:1 line is observed. By increasing the pressure beyond Δp_c^*, it is, of course, possible to access the nonlinear regime with any device. It is also worth mentioning that the flow rate tends to be approximately constant when the pressure ratio is increased beyond unity (see Appendix A). However, to mimic the action of a force-limited muscular pump [27], such as the heart, we constrain the pressure range in the subsequent analysis.

Another interesting observation is that the variations in the internal (organ) resistance $R^{(ij)}$ also had a strong impact on the flow. In particular, deviations from the linear flow behavior were not observed when the resistance ratio reached $\tilde{R} \geqslant 10$. This can be made apparent by considering the data in Fig. 3(b). For low relative resistance, $\tilde{R} \approx 10^{-4}$ (device 1 with resistor 0; see Table I), the sublinear flow-pressure characteristics deviate significantly from the 1:1 line. In contrast, when the internal resistance is increased to $\tilde{R} \approx 7$ (device 1 with resistor 3), no digression from the 1:1 line is observed. While the flow rate magnitude can be tuned at low internal resistance [Fig. 3(c), devices 1, 2, and 3 with resistor 0] by varying the channel width and height, an increase in organ resistance [$\tilde{R} \approx 4$–15, Fig. 3(d), devices 1, 2, and 3 with resistor 3] leads to the organ resistance-dominated regime where flow increases approximately linearly with applied pressure.
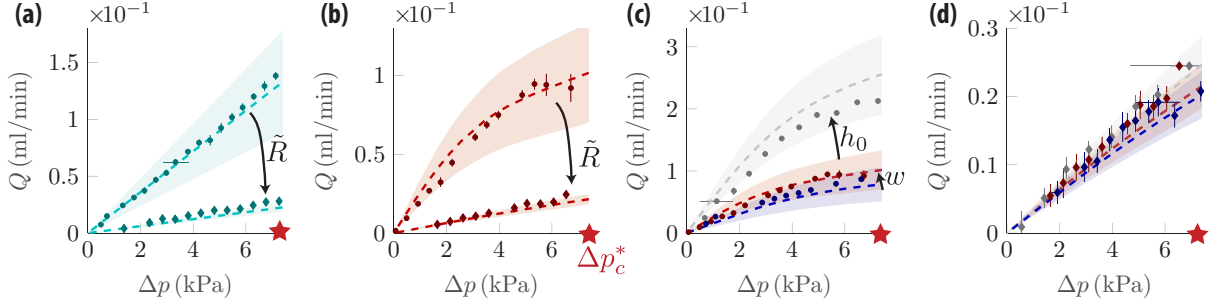
FIG. 3. Flow-to-pressure relationships for selected device configurations. Colors and symbols represent measurements for different device and internal resistance configurations; see Table I. Each shown $(\Delta p, Q)$ measurement consists of an average of 10 consecutive individual measurements. Error bars indicate the standard deviation. The dashed lines accompanying the measurements are our mathematical model, Eq. (27), with input parameters from Table I. The shaded regions around the dashed lines represent error propagation of the model, Eq. (27), using error estimates of the input parameters given in Table I. (a) Fluid device with a relatively thick elastic sheet (device 4, Table I). The resistance ratio is increased from $\tilde{R} \sim 10^{-4}$ to $\tilde{R} \approx 5$. (b) Fluid device with a relatively thick elastic sheet (device 1, Table I). The resistance ratio is increased from $\tilde{R} \sim 10^{-4}$ to $\tilde{R} \approx 7$. (c) Fluid devices with different channel height and width (devices 1, 2, and 3, Table I). $\tilde{R} \sim 10^{-4}$ in all three configurations. (d) Same as (c) but with $\tilde{R} \approx 4{-}15$.

We conclude this section with a general comment about the fluid flow conditions. Up to this point, we have argued that pressure-induced elastic deformations are responsible for the sublinear trends in the experimental data (Figs. 1 and 2). It is, however, well established that inertial effects can lead to similar patterns [28]. To estimate the magnitude of such effects in our setup, we calculated the Reynolds number Re $= (\rho \langle v \rangle h_0)/\mu \approx (0.5{-}1.0) \times 10^{-2}$, where $\langle v \rangle = Q/(2wh_0)$ is the average fluid velocity. This magnitude of Re suggests that inertial effects are not the primary driver of the observed data patterns.

IV. THEORY

To expand upon our understanding of the experimental observations and evaluate the feasibility of flow autoregulation under physiological conditions, we now proceed to develop a mathematical model. Our goal is to derive a relationship between the flow rate, Q, and the applied pressure drop across the fluidic device, Δp. We note that a full numerical solution to the coupled elastohydrodynamic problem is possible using, e.g., finite-element methods [29]. Here, however, we deliberately focus on a simpler approach with the limited goal of extracting key physical phenomena and parameter dependencies.

We begin by defining the governing equations. The fluid flow in the device inlet (i) and outlet (j) channels, and in the internal conduit (ij), are governed by the incompressible Navier-Stokes equation

$$\rho[\partial_t \mathbf{v} + (\mathbf{v} \cdot \nabla)\mathbf{v}] = -\nabla p + \mu \nabla^2 \mathbf{v} \tag{3}$$

and the continuity equation

$$\nabla \cdot \mathbf{v} = 0, \tag{4}$$

where $\mathbf{v}$ is the fluid velocity field and p is the pressure. The linear Kirchoff-Love equation governs the elastic sheet deformation [30,31]

$$\nabla_{\parallel}^2 \nabla_{\parallel}^2 u = \frac{p_t(x, z)}{D}, \tag{5}$$

where u is the sheet deformation, $\nabla_{\parallel}^2$ is the Laplace operator in the (x, z) plane [see Fig. 2(c)], and $D = \frac{E\tau^3}{12(1-\nu^2)}$ is the sheet's flexural rigidity. The transmural pressure, $p_t = p^{(i)} - p^{(j)}$, is the *local* position-dependent pressure difference between channels (i) and (j). As we advance, we label physical quantities (e.g., fluid velocity, pressure, dimensions) with superscripts (i), (j), and (ij) for channels (i), (j), and (ij), respectively.

In our experiments, the pressure was applied to the inlet of channel (i), and the pressure at the outlet of channel (j) was set to atmospheric. Since the outlet of channel (i) is connected to the inlet of channel (j) via the organ resistor where an intermediate pressure drop $\Delta p^{(ij)}$ is deposited, the pressure boundary conditions read

$$p^{(i)} = \Delta p \quad \text{and} \quad p^{(j)} = 0, \quad z = 0, \tag{6}$$

$$p^{(i)} - p^{(j)} = \Delta p^{(ij)} \quad z = \ell. \tag{7}$$

The no-slip fluid velocity boundary conditions in channels (i) and (j) require that

$$\mathbf{v}^{(i)}(x = \pm w, y, z) = \mathbf{v}^{(i)}\left(x, y = h_0^{(i)}, z\right)$$
$$= \mathbf{v}^{(i)}(x, y = -u(x, z), z) = \mathbf{0}, \tag{8}$$

$$\mathbf{v}^{(j)}(x = \pm w, y, z) = \mathbf{v}^{(j)}\left(x, y = -h_0^{(j)}, z\right)$$
$$= \mathbf{v}^{(j)}(x, y = -u(x, z), z) = \mathbf{0}. \tag{9}$$

Finally, the boundary conditions for the clamped membrane are

$$\partial_x u = u(x, z) = 0, \quad \text{at} \quad x = \pm w, \tag{10}$$

$$\partial_z u = u(x, z) = 0, \quad \text{at} \quad z = 0, \ell. \tag{11}$$

Having established the governing equations and boundary conditions, we continue our pursuit of a quantitative relation between the flow rate Q and pressure drop Δp. Before proceeding, however, we note that our equation system includes the undetermined internal pressure drop $\Delta p^{(ij)}$ [Eq. (7)]. In the following, we assume that it is linked to the organ flow $Q^{(ij)}$

rate via the Hagen-Poiseuille equation

$$Q^{(ij)} = \frac{\Delta p^{(ij)}}{R^{(ij)}}, \qquad (12)$$

where $R^{(ij)}$ is the internal hydraulic resistance. Moreover, an essential feature of our systems is the serial coupling of the inlet (i), organ (ij), and outlet (j) channels. Since the elastic sheet is impermeable, the fluid flow rate through the circuit is conserved, which leads to a statement of Kirchoff's current law in the form

$$Q \equiv Q^{(i)} = Q^{(ij)} = -Q^{(j)}. \qquad (13)$$

For each channel in the serial connection, the flow rate is computed by integrating the axis velocity component over the cross-sectional area (A). For example, the flow rate in the inlet channel (i) is

$$Q^{(i)} = \int_{-w}^{w} dx \int_{-u(x,z)}^{h_0^{(i)}} dy \, v_z^{(i)}(x, y, z). \qquad (14)$$

To determine the $Q - \Delta p$ relationship of the flow circuit, the velocity and pressure distribution is found for each conduit under the constraint of continuity [Eq. (13)]. This, however, is complicated by the two-way coupling of the fluid-elasticity problem. First, the sheet deformation u depends on the transmural pressure difference p_t [Eq. (5)]. Second, the fluid velocity and pressure distribution depend on the sheet deformation via the no-slip boundary conditions [Eqs. (8) and (9)]. To solve the coupled problem, we apply the standard approach (see, e.g., [32]) and use the following three-step procedure: First, we solve for the sheet deformation u given an arbitrary pressure profile p_t as input. Similarly, we compute the pressure and flow velocity for a given sheet deformation profile u. Finally, we apply the continuity constraint to determine a self-consistent pressure, flow, and deformation solution.

To enhance the physical clarity of the subsequent interpretation of our data, we begin by appropriately simplifying the governing equations for both the fluid and the elastic solid. The lubrication equations can approximate the fluid flow in channels (i) and (j) since the channels are shallow and long ($h_0^{(i,j)} \ll 2w \ll \ell$) and the Reynolds number is small, Re $\sim 10^{-2}$. This leads to

$$\partial_z p^{(i)}(z) = \mu \partial_y^2 v_z^{(i)} \quad \text{and} \qquad (15)$$

$$\partial_z p^{(j)}(z) = \mu \partial_y^2 v_z^{(j)}. \qquad (16)$$

The velocity and pressure boundary conditions [Eqs. (6) and (7)] are

$$v_z^{(i)} = 0 \quad \text{at} \quad y = h_0^{(i)} \quad \text{and} \quad y = -u, \qquad (17)$$

$$v_z^{(j)} = 0 \quad \text{at} \quad y = -h_0^{(j)} \quad \text{and} \quad y = -u. \qquad (18)$$

The sheet deformation can be approximated by the Euler-Bernoulli equation under the conditions that the deformations are relatively small ($u_{\max} = h_0 < \tau$) and that the sheet is thin and long ($\tau \ll 2w \ll \ell$),

$$\partial_x^4 u = \frac{p_t(z)}{D}. \qquad (19)$$

It is worth noting that by disregarding the effects of the axial z coordinate, we have also ignored the potential end effects.

The membrane corners, however, are located away from the overlapping flow channel and are thus likely, at least to a first approximation, to play a relatively small role in determining the deflection. Finally, the elastic boundary conditions are

$$u(x, z) = \partial_x u(x, z) = 0 \quad \text{at} \quad x = \pm w. \qquad (20)$$

Conveniently, the sheet deformation is now governed by an ordinary differential equation in x [Eq. (19)] even though the transverse pressure difference has an implicit z dependency [Eqs. (15) and (16)]. This allows us to solve for the deformation u while treating the transmural pressure p_t as constant and for the flow velocities, $v_z^{(i)}$ and $v_z^{(j)}$, while treating the deformation u as constant. Using this approach, we find the usual fourth-order sheet deformation profile

$$u(x, z) = h_0^{(j)} \frac{p_t(z)}{\Delta p_c} \left(1 - \frac{x}{w}\right)^2 \left(1 + \frac{x}{w}\right)^2, \qquad (21)$$

where $\Delta p_c = \frac{24 D h_0^{(j)}}{w^4}$ is the contact pressure at which the maximum deformation $u(x = 0) = h_0^{(j)}$ equals the height of outlet channel (j). Next, it emerges that the flow velocities are of the usual parabolic form

$$v_z^{(i)} = \frac{1}{2\mu} \partial_z p^{(i)} \left(y - h_0^{(i)}\right)(y + u(x, z)), \qquad (22)$$

$$v_z^{(j)} = \frac{1}{2\mu} \partial_z p^{(j)} \left(y + h_0^{(j)}\right)(y + u(x, z)). \qquad (23)$$

Finally, this allows us to calculate the inlet and outlet conduit flow rates

$$Q^{(i)} = -\frac{\ell}{R_0^{(i)}} \partial_z p^{(i)} f[\epsilon p_t(z)/p_c], \qquad (24)$$

$$Q^{(j)} = -\frac{\ell}{R_0^{(j)}} \partial_z p^{(j)} f[-p_t(z)/p_c], \qquad (25)$$

where $R_0^{(i)} = \frac{12\mu\ell}{2w(h_0^{(i)})^3}$ and $R_0^{(j)} = \frac{12\mu\ell}{2w(h_0^{(j)})^3}$ are the base resistances of channels (i) and (j), respectively, corresponding to the undeformed geometry. The parameter $\epsilon = h_0^{(i)}/h_0^{(j)}$ is the ratio of the channel (i) and (j) heights (note that in our experiments, $\epsilon = 1$), and the function $f(s)$ is the polynomial

$$f(s) = 1 + \frac{8}{5}s + \frac{128}{105}s^2 + \frac{1048}{3003}s^3, \qquad (26)$$

where the coefficients stem from the integration of the lubrication equations.

Before proceeding with our exploration of the $\Delta p - Q$ relation, we note that a closed-form solution to Eq. (13) was found by Christov *et al.* [32] for pressure-driven flow in a single rectangular duct with an elastic lid (see also the related work by members of our team on individual compliant channels [33]). In the present study, however, the two channels interact via a shared soft boundary, and the flow rate in channel (i) depends on the pressure in both channels (i) and (j), and vice versa for channel (j). This complicates efforts to determine a similar closed-form expression for the flow rate, and it is not, to our knowledge, generally possible. However, robust numerical solutions can be determined by employing, e.g., a basic finite-difference method, thereby revealing the $Q - \Delta p$ relationship for a specific choice of parameters (see Appendix B).

TABLE II. The pressure-drop vs flow-rate relationship [Eq. (27)] in the limits of low resistance ($\tilde{R} \ll 1$), high resistance ($\tilde{R} \gg 1$), low pressure ($\tilde{P} \ll 1$), and high pressure ($\tilde{P} \sim 1$).

	$\tilde{R} \ll 1$	$\tilde{R} \gg 1$
$\tilde{P} \ll 1$	$\frac{\Delta p}{2R_0}$	$\frac{\Delta p}{R^{(ij)}}$
$\tilde{P} \sim 1$	$\frac{\Delta p}{2R_0}(1 - 0.7\tilde{P} + 0.2\tilde{P}^2)$	$\frac{\Delta p}{R^{(ij)}}$

To unpack the basic dependence on physical parameters in our data, we leave the detailed numerical analysis to future works and focus instead on an approximate analytical solution. This, it turns out, is most conveniently developed starting in the limit of large internal resistance ($\tilde{R} \gg 1$). To separate ourselves from nonessential mathematical complications, we further limit our attention to the experimental case at hand, in which the inlet and outlet channels have equal heights, thereby fixing the parameter $\epsilon = h_0^{(i)}/h_0^{(j)} = 1$. (This implies that the base resistances are equal, i.e., $R_0 \equiv R_0^{(i)} = R_0^{(j)}$.) Since we assume the resistance ratio is large, the majority of the pressure drop is deposited across the organ resistor, and we can approximate the transmural pressure as $p_t(z) \approx \Delta p$, i.e., independent of the longitudinal position z. This results in the sheet deformation being independent of z, which allows us to integrate Eqs. (24) and (25) using the pressure boundary conditions in Eqs. (6) and (7). Then, combining the resulting flow rates $Q^{(i)}$ and $Q^{(j)}$ with the organ flow rate in Eq. (12), the solution to the circuit equation (13), reads

$$Q = \frac{\Delta p}{R_0} \frac{1}{2\tilde{R} + f^{-1}(\tilde{P}) + f^{-1}(-\tilde{P})}, \qquad (27)$$

where the function f is defined in Eq. (26). This result differs from the numerics by less than 30% even when the resistance ratio is small, $\tilde{R} \sim 0.1$. However, the error is already reduced to approximately 10% for moderate resistance ratios $\tilde{R} \sim 1$, and further decreased to less than 5% when the resistance ratio $\tilde{R} \sim 10$.

To elucidate the physical meaning of the flow-rate relation in Eq. (27), we first note that the result is consistent with the equivalent rigid system by setting $\tilde{P} = \Delta p/\Delta p_c \ll 1$, which yields a linear pressure-flow relation

$$Q_0 = \frac{\Delta p}{2R_0(1 + \tilde{R})}, \quad (\text{for } \Delta p_c \ll \Delta p). \qquad (28)$$

The remaining two terms $f(\tilde{P})$ and $f(-\tilde{P})$ in the denominator of Eq. (27) contain the effect of the opening inlet channel ($f(\tilde{P}) > 1$) and the closing outlet conduit [$f(-\tilde{P}) < 1$].

The functional form for the pressure-drop vs flow-rate relation can best be appreciated by performing a series expansion of the flow rate Q in Eq. (27) (Table II). For low internal resistance ($\tilde{R} \ll 1$), the flow is dominated by the overlap resistance $2R_0 = R_0^{(i)} + R_0^{(j)}$. In contrast, in the opposite limit ($\tilde{R} \gg 1$), the flow resistance is dominated by the organ resistance $R^{(ij)}$. On the other hand, at relatively high pressures ($\tilde{P} \approx 1$), the flow rate depends nonlinearly on applied pressure when the resistance $\tilde{R} \ll 1$ is small. In this limit, the flow rate $Q \sim \Delta p/R_0(1 - 0.7\tilde{P} + 0.2\tilde{P}^2)$ deviates substantially from the linear trend.
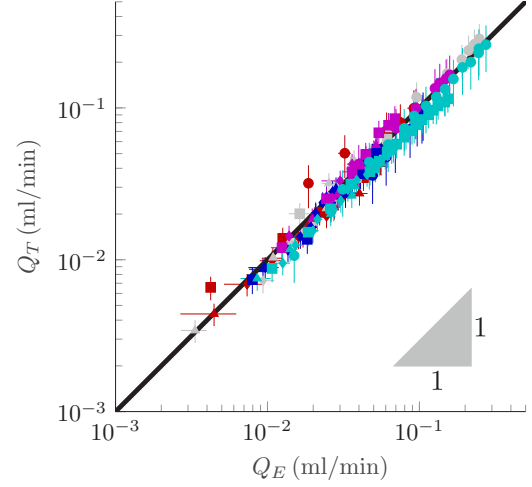

FIG. 4. Lubrication model flow rates (Q_T) vs experimentally measured flow rates (Q_E). (x, y) error bars indicate standard deviation in flow rate measurements and error propagation in the lubrication model [Eq. (27)] with parameters in Table I. The solid black line indicates a 1:1 relationship.

V. DISCUSSION

To evaluate the ability of the model to rationalize the data, we have superposed the measurements in Fig. 3 with the model using the parameters and color or symbol encoding in Table I. The dashed colored lines correspond to Eq. (27) with no free parameters. The shaded regions around the lines in Fig. 3 correspond to error propagation of Eq. (27) with respect to uncertainties in measured geometrical and material parameters. (We note that the model is relatively sensitive to small variations in geometrical and material parameters because, for instance, the hydraulic resistance scales with the inverse cube of the channel height.) Across our experiments, we find reasonable agreement with theory (Figs. 3 and 4). Notably, the juxtaposition of data and theory lends credence to a simple physical picture: Autoregulation is possible if the applied pressure is sufficient to deform the overlapping conduits, and if the internal resistance of the system is not too great. The potential efficacy of the autoregulation process and the relevance of this mechanism to physiological flows is discussed in the following section.

A. Autoregulation efficiency

To quantify the autoregulatory efficiency of flow across overlapping channels, it is fitting to compare the slope of the flow rate Q [Eq. (27)] to the rigid-pipe limit Q_0 [Eq. (28)]. We therefore introduce the *differential conductance ratio*

$$\mathcal{C} = \frac{Q'}{Q_0'}, \qquad (29)$$

where the primes denote differentiation with respect to the applied pressure drop Δp. When $\mathcal{C} \ll 1$ is small, the deformation-induced autoregulation mechanism imposes a comparatively constant current through the system ($Q \approx$ const), irrespective of the applied pressure. In contrast, when
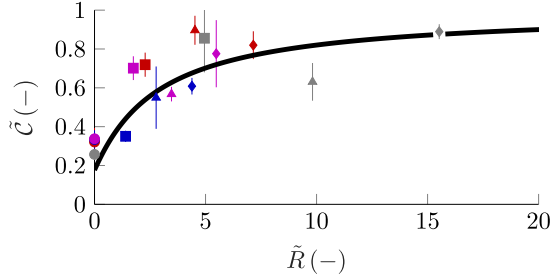
FIG. 5. Elastohydrodynamic autoregulation efficiency $\tilde{\mathcal{C}}$ [Eq. (30)] plotted as a function of the resistance ratio $\tilde{R}$. Measured values of $\tilde{\mathcal{C}}$ are labeled according to Table I.

$\mathcal{C} \approx 1$, the pressure-drop vs flow-rate relation follows the rigid pipe system ($Q = Q_0$).

The magnitude of the differential conductance ratio $\mathcal{C}$, depends on the applied pressure Δp and on the geometric and material parameters. It is, however, apparent from Fig. 3(b), that the strongest effect is obtained at or near the contact pressure $\Delta p = \Delta p_c$. To evaluate the potential for smoothing in an organ, we therefore consider the magnitude of the differential conductance ratio $\tilde{\mathcal{C}}$ at this point. Using Eqs. (27) and (28) leads to

$$\tilde{\mathcal{C}} = \mathcal{C}(\tilde{P} = 1, \tilde{R}) = \frac{(\tilde{R} + A)(\tilde{R} + 1)}{(\tilde{R} + B)^2}, \quad (30)$$

where $A \approx 0.69$ and $B \approx 1.97$ are pure numbers independent of geometry and materials, and $\tilde{R}$ is the resistance ratio. The smallest differential conductance ratio $\tilde{\mathcal{C}} \approx 0.18$ is achieved when the resistance ratio vanishes, $\tilde{R} = 0$, while it approaches 1 asymptotically as the resistance increases [Fig. 5(b)].

To test the predicted relation between $\tilde{\mathcal{C}}$ [Eq. (30)] and system parameters, we directly computed Q' and Q'_0 from our experiments from linear fits to the high- and low-pressure data (i.e., at $\tilde{P} \approx 1$ and $\tilde{P} \approx 0$, respectively). The measured differential conductance ratios are not inconsistent with the model (Fig. 5).

B. Application to physiological flow conditions

We end our analysis by exploring the feasibility of overlapping channels as an autoregulatory mechanism under physiological conditions (Fig. 1). In the preceding analysis, we identified two key physical conditions which must be met for physiologically relevant flow control to occur. First, the overlapping tube segment should be soft: The applied pressure Δp must exceed approximately half the stress Δp_c required for the tissue to deform significantly [e.g., Fig. 3(b)]. Second, the hydraulic resistance of the organ or tissue $R^{(ij)}$ should be no greater than ten times that of the overlapping segment $R_0^{(i)} + R_0^{(j)} = 2R_0$ for autoregulation to occur (Fig. 5).

It is difficult to ascertain whether these criteria are met based on data available on anatomical features and material properties, At this point, we, therefore cannot draw definite conclusions on the occurrence of the proposed autoregulation mechanism. We are, however, able to explore the process' feasibility based on literature data. Indeed, vascular pressure and tissue properties have been widely studied, and in many animals, blood pressure typically falls in the range 10^3–10^4 Pa
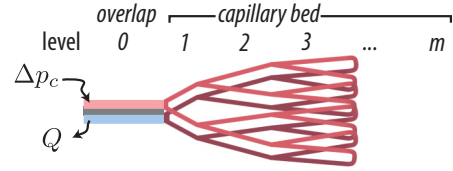
[34]. The elastic modulus E of several soft mammal tissues also overlaps with this range $E \sim 10^3$–10^4 Pa (e.g., brain and lung); however, the stiffness of, e.g., connective tissues can be much larger ($E \sim 10^9$ Pa for tendons) [35]. The first criterion ($\Delta p \approx \Delta p_c$) is thus met in some, but of course not all, tissues.

To explore whether the organ or tissue resistance is comparable to that of a potential conduit overlap, we first note that experimental data on the hydraulic resistance of whole organs (or hydraulically isolated embedded subunits) are scarce. To proceed, we, therefore, develop an approximate tissue model based on Murray's law of a branching network [36–38]; see Fig. 6. We begin at the inlet by one of the overlapping segments of diameter d_0 and length L. The diameter of subsequent N daughter branches related to parent branches via Murray's law

$$\frac{d_k}{d_{k-1}} = N^{-1/3} \quad \text{for} \quad k = 1, \ldots, m, \quad (31)$$

where m is the depth of the network and the power $1/3$ assumes that the network is Murray-optimized to minimize the total power dissipation. The total hydraulic resistance of the network linking the two overlapping channels is

$$R^{(ij)} = 2\sum_{k=1}^{m} \frac{1}{N^k} \frac{128\eta L}{\pi d_k^4} = \frac{256\eta L}{\pi d_0^4} \frac{N^{1/3}(N^{m/3} - 1)}{N^{1/3} - 1}, \quad (32)$$

calculated based on the Hagen-Poiseuille law under low-Reynolds-number conditions. Note the prefactor of 2 in Eq. (32), which represents that the network first branches form an individual conduit into many and then from many back into a single channel [Fig. 5(a)]. We also note that Eq. (32) assumes constant branch length L. It is possible to relax this condition [39], but we will not do that here.

The relative significance of tissue and overlap resistance can be captured by considering the ratio of the two given by the parameter $\tilde{R}$ [Eq. (2)]:

$$\tilde{R}(N, m) = \frac{R^{(ij)}}{2R_0} = N^{1/3} \frac{N^{m/3} - 1}{N^{1/3} - 1}. \quad (33)$$

From Eq. (33) it is apparent that resistance ratio $\tilde{R}$ varies nonlinearly with the branching number N, and the capillary bed depth m. In mammalian circulatory systems, each branching layer typically adds $N < 10$ daughter conduits, and the capillary bed depth varies from $m = 1$ (a single channel overlapping with itself) to $m \approx 10$ starting near the heart. Recall that a low value of m indicates local autoregulation (i.e., few network layers in the organ or limb), and a high value of m indicates that the vessel overlap supplies or carries out waste from a deep capillary bed. In any case, the resistance ratio increases with both branching number (N) and depth (m). Therefore, with the parameters estimated above,

FIG. 6. Organ capillary tree model based on Murray's law.

the highest value of $\tilde{R} \sim 10^3$ is found with, say, $N = 7$ and $m = 10$. This example could approximate autoregulation in extremities (e.g., toes or fingers) by a vessel overlap close to the heart. However, with $\tilde{R} \sim 10^3$ the corresponding differential conductance ratio is close to unity, $\tilde{C} \approx 1$, and passive autoregulation is not feasible. On the other hand, the lowest value of $\tilde{R} \approx 2.85$ is found when $N = 2$ and $m = 2$, depicting autoregulation by overlapping vessels at the entrance to an organ with relatively few branches. In that case, the relatively small differential conductance ratio, $\tilde{C} \approx 0.58$, suggests that passive autoregulation is feasible. The variation of the differential conductance ratio $\tilde{C}$ with resistance for different capillary networks is illustrated in Fig. 5(b).

To explore the significance of the differential conductance ratio we will consider it in relation to the human kidney glomerulus. This structure plays a crucial role in filtering blood, and it is plausible that it utilizes passive flow autoregulation to carry out its function. More specifically, the renal arterial tree delivers blood to the kidney, starting with the sizable renal artery and branching out into smaller vessels [40]. Within this intricate network are the afferent arterioles that supply the glomerulus, which is then drained by the efferent arterioles. Notably, these two arterioles are situated in close proximity near the Bowman's capsule opening, creating the potential for the passive autoregulation process expounded upon in this article. To quantify the differential conductance ratio for this afferent-efferent arteriole pair, we will assume that the pressure drop across them is large enough such that elastohydrodynamic interactions can occur (i.e., the pressure ratio is close to unity) and that the branching in the glomerulus network follows Murray's law. This allows using Eqs. (30) and (33) to quantify the corresponding differential conductance ratio. Since the glomerulus network is small, we can estimate its depth as $m = 2$–3. With a branching number of $N = 2$, injecting these values into Eqs. (33) and (30) results in a differential conductance ratio range of $\tilde{C} = 0.59$–0.70, which is within the necessary range for passive autoregulation.

VI. CONCLUSION

Fluid flow autoregulation is critical for maintaining a steady nutrient supply in many living systems. While flow control is presently ascribed to active processes, this paper explores the possibility of an alternative elastohydrodynamic process. Inspired by Starling's resistor, we have built a passive fluidic device that comprises two linked channels separated by an elastic sheet. The pressure difference between the two overlapping channels causes one to dilate and the other to compress. This fluid-structure interaction causes the overall conductance to decrease with increasing pressure, thus leading to an entirely passive flow-limiting autoregulatory mechanism. To quantify the efficacy of the flow control process, we introduced the differential conductance ratio $\tilde{C}$. This nondimensional quantity compares the differential conductance in a soft conduit network to that of a rigid conduit system. Small values of $\tilde{C}$ correspond to successful flow control. Our results, which include experiments and modeling, reveal that this regime is accessible when the pressure is sufficient to deform the tissue and when the organ resistance is not too large. While compliant vessels have the potential for self-regulating
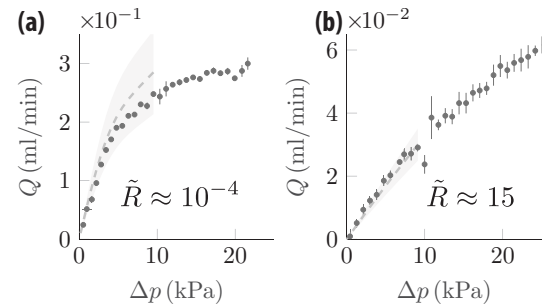

FIG. 7. Measured flow-vs-pressure relationship for device 2 beyond the contact pressure ($p_c \approx 10$ kPa). In (a) the resistance ratio is $\tilde{R} \approx 10^{-4}$, and in (b) the resistance ratio is $\tilde{R} \approx 15$.

fluid flow, the physiological relevance of the proposed process remains unclear. To test this hypothesis, additional data related to the arrangement of conduits and their mechanical properties near the entrance to critical organs are required.

APPENDIX A: FLOW CAPACITY WHEN APPLIED PRESSURE EXCEEDS THE CONTACT PRESSURE

This Appendix outlines observations on flow rate capacity when the applied pressure exceeds the contact pressure obtained via linear plate theory. It should be noted that our mathematical model presented in Sec. IV is valid only in the pressure range $\tilde{P} = 0$–1 and breaks down when the applied pressure exceeds the contact pressure (at $\tilde{P} = 1$). In our experiments, however, we were able to apply pressure beyond the contact pressure, up to $\tilde{P} \approx 2.5$, before the onset of leakages from the fluid devices. We show measurements of the flow-rate-pressure-drop relationship for our device 2 (Fig. 7). When the resistance ratio is relatively small ($\tilde{R} \approx 10^{-4}$), the postcontact pressure flow rate tends to a constant [Fig. 7(a)]. However, for a relatively large resistance ratio ($\tilde{R} \approx 15$), the flow rate remains close to linear with an increasing applied pressure. It is not inconceivable that the large-resistance-ratio experiment could access a stronger nonlinear regime, albeit at much larger pressure when the compressed channel's aperture is decreased significantly.

APPENDIX B: NUMERICAL FLOW-PRESSURE RELATIONSHIP SOLUTION

This Appendix outlines a numerical scheme to solve the coupled flow-pressure equations in two overlapping soft channels (i) and (j) connected via a resistor (ij). Pressure is applied to the inlet of channel (i), and the outlet of channel (j) is connected to atmospheric pressure. We seek to solve the flow-pressure relationship of the serial connection between channels (i), (j), and (ij). Flow continuity is enforced by

Eq. (13), and the flow rates through each channel are given by Eqs. (12), (24), and (25). The pressure boundary conditions are given by Eqs. (6) and (7).

The flow rates in channels (i) and (j) are coupled since they both depend on the transmural pressure difference $p_t(z) = p^{(i)}(z) - p^{(j)}(z)$. To find a numerical solution to the flow conservation equation, we will apply a finite-difference method (FDM) scheme that iteratively approximates the pressure drops in channels (i) and (j). From Eqs. (24) and (25) we have that

$$\frac{p^{(i)}(z + \Delta z) - p^{(i)}(z)}{\Delta z} \approx \frac{\partial p^{(i)}}{\partial z} = -\frac{Q^{(i)} R_0^{(i)}}{\ell f(\epsilon p_t(z)/p_c)}, \quad \text{(B1)}$$

$$\frac{p^{(j)}(z + \Delta z) - p^{(j)}(z)}{\Delta z} \approx \frac{\partial p^{(j)}}{\partial z} = -\frac{Q^{(j)} R_0^{(j)}}{\ell f(-\epsilon p_t(z)/p_c)}, \quad \text{(B2)}$$

where $R_0^{(i)} = \frac{12 \mu \ell}{2w(h_0^{(i)})^3}$ and $R_0^{(j)} = \frac{12 \mu \ell}{2w(h_0^{(j)})^3}$ are the base resistances of channel i and j, respectively, corresponding to the undeformed geometry. The function $f(x)$ is given in Eq. (26). The parameter $\epsilon = h_0^{(i)}/h_0^{(j)}$ links the channel heights in channels (i) and (j). The channel height ratio $\epsilon = h_0^{(i)}/h_0^{(j)}$ links channels (i)'s and (j)'s. Note also that $p_t(z) = p^{(i)}(z) - p^{(j)}(z)$ coupling Eqs. (B1) and (B2). Rearranging Eqs. (B1) and (B2) allows us to approximate the pressures as

$$p^{(i)}(z + \Delta z) = p^{(i)}(z) - \Delta z \frac{Q^{(i)} R_0^{(i)}}{\ell f[\epsilon(p_t(z))/p_c]}, \quad \text{(B3)}$$

$$p^{(j)}(z + \Delta z) = p^{(j)}(z) + \Delta z \frac{Q^{(j)} R_0^{(j)}}{\ell f[-(p_t(z))/p_c]}, \quad \text{(B4)}$$

which provide explicit approximations for the pressure gradients in channels (i) and (j).

The finite-difference method scheme is initiated by discretizing channels (i) and (j) into small pieces, $\Delta z = \ell/1000$. For an initial guess of the flow rate, Q [given by Eq. (13)], and a specific choice of input pressure Δp, the pressures in channels (i) and (j) are initialized as linearly decreasing [starting at $p^{(i)}(0) = \Delta p$] and increasing [starting at $p^{(j)}(0) = 0$], consistent with the pressure boundary conditions in Eq. (6). The initial guess of the flow rate Q also sets the pressure drop across the bypass resistor via $\Delta p^{(ij)} = QR^{(ij)}$. Hence, the other pressure boundary condition [Eq. (7)] can be formulated as the residual of the parameter δ:

$$\delta = |p^{(i)}(\ell) - p^{(j)}(\ell) - QR^{(ij)}|. \quad \text{(B5)}$$

For the specific choice of applied pressure Δp, the pressure residual in Eq. (B5) is minimized with respect to flow rate Q, using the MATLAB programming solver *fminsearch*. Once the flow rate that satisfies the pressure boundary conditions is found, the algorithm is run again for a new value of applied pressure, Δp. Starting at $\Delta p = 0$, we sweep in applied pressure until the contact pressure $\Delta p = p_c$ is reached [or, in terms of the pressure ratio, from $\tilde{P} = 0$ to $\tilde{P} = 1$; see Eq. (1)]. Setting the channels heights (and widths and lengths) in channels (i) and (j) equal, meaning that $\epsilon = 1$ and $R_0^{(i)} = R_0^{(j)}$, allows us to compare the numerical solution to the approximated analytical solution [Eq. (27)]. We compare the solutions for different pressure ratio values and resistance ratio values [Eqs. (1) and (2), respectively]. The resistance
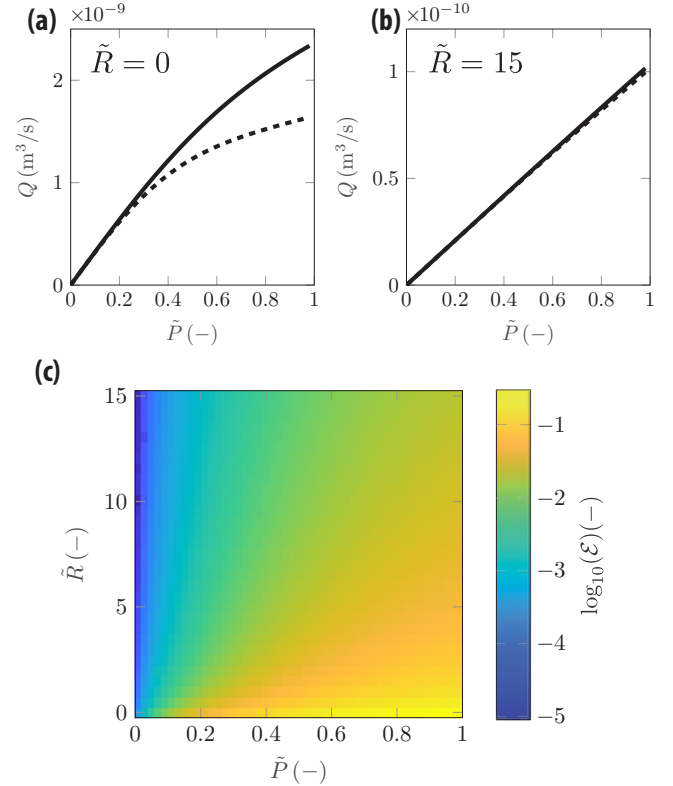

FIG. 8. Flow-vs-pressure relationship computed via the finite-difference method [Eqs. (B1) and (B2)] and our approximate analytical solution [Eq. (27)]. (a), (b) The finite-difference method solution (black solid line) and the analytical solution [black dashed line; Eq. (27)] with resistance ratio (a) $\tilde{R} = 0$ and (b) $\tilde{R} = 15$. (c) Logarithm of the discrepancy $\mathcal{E}$ between the numerical and analytical solutions [Eq. (B6)] for the pressure range $\tilde{P} = 0 - 1$ and resistance $\tilde{R} = 0$–15.

ratio enters the numerical solution via $R^{(ij)}$ in the pressure residual, Eq. (B5). To unpack the differences and similarities between the numerical and analytical solutions, we will consider the relative discrepancy

$$\mathcal{E}(\tilde{P}, \tilde{R}) = (Q_{\text{num}} - Q_{\text{an}}/Q_{\text{num}}) \quad \text{(B6)}$$

between the numerical solution Q_{num} and the analytical solution Q_{an} which is a function of the pressure ratio $\tilde{P}$ and the resistance ratio $\tilde{R}$. At low applied pressure, $\tilde{P} \approx 0$, both the numerical and analytical solutions yield approximately linear relationships between flow and pressure [Figs. 8(a) and 8(b)] regardless of resistance ratio. At relatively high applied pressure, $\tilde{P} \approx 1$ and low resistance ratio, $\tilde{R} = 0$, both the numerical and analytical flow-pressure relationships deviate from linear [Fig. 8(a)]. The critical pressure at which the deviation from linear flow-pressure characteristics sets in is lower for the approximate analytical model compared to the numerical solution [Fig. 8(a)], which leads to the relatively large discrepancy between the two solutions of $\mathcal{E} \approx 0.3$. For intermediate values of pressure ($\tilde{P}$) and resistance ($\tilde{R}$), the discrepancy varies between $\mathcal{E} \approx 10^{-4}$–$10^{-1}$ and is largest for high pressure and low resistance, and smallest for low pressure and (or) high resistance [Fig. 8(c)].

[1] M. Heil and A. L. Hazel, Fluid-structure interaction in internal physiological flows, Annu. Rev. Fluid Mech. **43**, 141 (2011).

[2] W. M. Bayliss, On the local reactions of the arterial wall to changes of internal pressure, J. Physiol. **28**, 220 (1902).

[3] P. C. Johnson and M. Intaglietta, Contributions of pressure and flow sensitivity to autoregulation in mesenteric arterioles, Am. J. Physiol. Legacy Content **231**, 1686 (1976).

[4] B. Folkow, Intravascular pressure as a factor regulating the tone of the small vessels, Acta Physiol. Scand. **17**, 289 (1949).

[5] W. Halpern and G. Osol, Influence of transmural pressure on myogenic responses of isolated cerebral arteries of the rat, Ann. Biomed. Eng. **13**, 287 (1985).

[6] K. Aukland, Myogenic mechanisms in the kidney, J. Intl. Soc. Hypert. **7**, S71 (1989).

[7] W. Lautt, Mechanism and role of intrinsic regulation of hepatic arterial blood flow: Hepatic arterial buffer response, Am. J, Physiol.-Gastroint. Liver Physiol. **249**, G549 (1985).

[8] R. Klabunde, *Cardiovascular Physiology Concepts* (Lippincott Williams & Wilkins, Philadelphia, PA, 2011).

[9] R. Higashida, G. Hieshima, V. Halbach, J. Bentson, and K. Goto, Closure of carotid cavernous sinus fistulae by external compression of the carotid artery and jugular vein, Acta Radiol. Suppl. **369**, 580 (1986).

[10] A. C. M. Amato and N. A. G. Stolf, Preoperative assessment of the spinal cord vasculature, in *Visceral Vessels and Aortic Repair*, edited by Y. Tshomba, R. Chiesa, and D. Baccellieri (Springer, Berlin, 2019), pp. 285–295.

[11] H. Aoki, H. Takagane, Y. Banya, T. Fujioka, K. Seo, T. Kubo, and T. Ohhori, Human penile hemodynamics studied by a polarographic method, J. Urol. **135**, 872 (1986).

[12] R. May and J. Thurner, The cause of the predominantly sinistral occurrence of thrombosis of the pelvic veins, Angiology **8**, 419 (1957).

[13] J. Ferda, M. Hora, O. Hes, E. Ferdová, and B. Kreuzberg, Assessment of the kidney tumor vascular supply by two-phase MDCT-angiography, Eur. J. Radiol. **62**, 295 (2007).

[14] H. Aoki, J. Matsuzaka, Y. Banya, T. Fujioka, S. Nakaya, T. Kubo, T. Ohhori, and N. Yasuda, Effects of hypogastric nerve and sympathetic chain stimulation on the pelvic nerve induced penile erection in the dog, Urol. Int. **47**, 25 (1991).

[15] A. K. Kurklinsky and T. W. Rooke, Nutcracker phenomenon and nutcracker syndrome, in *Mayo Clinic Proceedings*, edited by W. L. Lanier (Elsevier, Rochester, MN, 2010), Vol. 85, pp. 552–559.

[16] T. Pedley, G. Batchelor, H. Moffatt, and M. Worster, Blood flow in arteries and veins, in *Perspectives in Fluid Dynamics: A Collective Introduction to Current Research*, edited by G. K. Batchelor, H. K. Moffatt, and M. G. Worster (Cambridge University Press, Cambridge, UK, 2000), p. 105.

[17] F. Knowlton and E. Starling, The influence of variations in temperature and blood-pressure on the performance of the isolated mammalian heart, J. Physiol. **44**, 206 (1912).

[18] J. Holt, The collapse factor in the measurement of venous pressure: The flow of fluid through collapsible tubes, Am. J. Physiol. Legacy Content **134**, 292 (1941).

[19] S. Rubinow and J. B. Keller, Flow of a viscous fluid through an elastic tube with applications to blood flow, J. Theor. Biol. **35**, 299 (1972).

[20] C. Bertram, Experimental studies of collapsible tubes, in *Flow Past Highly Compliant Boundaries and in Collapsible Tubes*, edited by P. W. Carpenter and T. J. Pedley (Springer, Dordrecht, 2003), pp. 51–65.

[21] C. Lyon, J. Scott, and C. Want, Flow through collapsible tubes at low Reynolds numbers, Circ. Res. **47**, 68 (1980).

[22] C. Bertram and J. Tscherry, The onset of flow-rate limitation and flow-induced oscillations in collapsible tubes, J. Fluids Struct. **22**, 1029 (2006).

[23] G. A. Brecher, Mechanism of venous flow under different degrees of aspiration, Am. J. Physiol. Legacy Content **169**, 423 (1952).

[24] S. Rodbard, Autoregulation in encapsulated, passive, soft-walled vessels, Am. Heart J. **65**, 648 (1963).

[25] I. Johnston, D. McCluskey, C. Tan, and M. Tracey, Mechanical characterization of bulk Sylgard 184 for microfluidics and microengineering, J. Micromech. Microeng. **24**, 035017 (2014).

[26] B. Lautrup, *Physics of Continuous Matter: Exotic and Everyday Phenomena in the Macroscopic World* (CRC Press, 2011).

[27] W. Kim and J. W. Bush, Natural drinking strategies, J. Fluid Mech. **705**, 7 (2012).

[28] L. Prandtl and O. G. Tietjens, *Applied Hydro- and Aeromechanics: Based on Lectures of L. Prandtl* (Dover Publications, 1957).

[29] D. Chakraborty, J. R. Prakash, J. Friend, and L. Yeo, Fluid-structure interaction in deformable microchannels, Phys. Fluids **24**, 102002 (2012).

[30] L. D. Landau, E. M. Lifšic, E. M. Lifshitz, A. M. Kosevich, and L. P. Pitaevskii, *Theory of Elasticity*, Course of Theoretical Physics Vol. 7 (Elsevier, Amsterdam, 1986).

[31] E. S. Ventsel and T. Krauthammer, *Thin Plates and Shells: Theory, Analysis, and Applications* (Marcel Dekker, 2001).

[32] I. C. Christov, V. Cognet, T. C. Shidhore, and H. A. Stone, Flow rate–pressure drop relation for deformable shallow microfluidic channels, J. Fluid Mech. **841**, 267 (2018).

[33] M. D. Biviano, M. V. Paludan, A. H. Christensen, E. V. Østergaard, and K. H. Jensen, Smoothing Oscillatory Peristaltic Pump Flow with Bioinspired Passive Components, Phys. Rev. Appl. **18**, 064013 (2022).

[34] K. Schulte, U. Kunter, and M. J. Moeller, The evolution of blood pressure and the rise of mankind, Nephrol Dialysis Transplant **30**, 713 (2015).

[35] G. Singh and A. Chanda, Mechanical properties of whole-body soft human tissues: A review, Biomed. Mater. **16**, 062004 (2021).

[36] C. D. Murray, The physiological principle of minimum work: I. The vascular system and the cost of blood volume, Proc. Natl. Acad. Sci. USA **12**, 207 (1926).

[37] C. D. Murray, The physiological principle of minimum work: II. Oxygen exchange in capillaries, Proc. Natl. Acad. Sci. USA **12**, 299 (1926).

[38] T. F. Sherman, On connecting large vessels to small. the meaning of Murray's law, J. Gen. Physiol. **78**, 431 (1981).

[39] P. Xu, A. P. Sasmito, B. Yu, and A. S. Mujumdar, Transport phenomena and properties in treelike networks, Appl. Mech. Rev. **68**, 040802 (2016).

[40] J. E. Hall and M. E. Hall, *Guyton and Hall Textbook of Medical Physiology e-Book* (Elsevier Health Sciences, 2020).